Published in final edited form as:
Aerosol Sci Technol. 2013 February 1; 47(2): 169–176. doi:10.1080/02786826.2012.735380.

Arsenic removal from water using flame-synthesized iron oxide nanoparticles with variable oxidation states

Aamir D. Abid[†], **Masakazu Kanematsu**[‡], **Thomas M. Young**[‡], and **Ian M. Kennedy**[†,*]

[†]Department of Mechanical and Aerospace Engineering, University of California Davis, One Shields Avenue, Davis, California 95616, U.S.A.

[‡]Department of Civil and Environmental Engineering, University of California Davis

Abstract

We utilized gas-phase diffusion flame synthesis, which has potential for large-scale production of metal oxide nanoparticles, to produce iron oxide nanoparticles (IONPs) with variable oxidation states. The efficacy of these materials in removal of arsenate (As(V)) from water was assessed. Two different flame configurations, a diffusion flame (DF) and an inverse diffusion flame (IDF), were employed to synthesize six different IONPs by controlling flame conditions. The IONPs produced in the IDF configuration (IDF-IONPs) had smaller particle diameters (4.8 – 8.2 nm) and larger surface areas (141–213 m^2/g) than the IONPs produced in the DF configuration (29 nm, 36 m^2/g), which resulted in their higher adsorption capacities. As(V) adsorption capacities of the IDF-IONPs increased when the IONPs were synthesized in more oxidizing conditions. The fully oxidized IDF-IONPs, maghemite (γ-Fe_2O_3), showed the highest As(V) adsorption capacity, comparable to that of magnetite nanocrystals synthesized by thermal decomposition of iron pentacarbonyl and equivalent to three to four times higher capacity than that of a commonly used goethite-based adsorbent. All IONPs were magnetically responsive, which is of great importance for solid−liquid separation. This study demonstrates that the IONPs synthesized in gas-phase flame, particularly IDF-IONPs, are excellent adsorbents because of their high As(V) sorption capacity, potential for large-scale production, and useful magnetic property.

Introduction

Arsenic in drinking water poses a significant health risk to human beings across the globe (Nordstrom 2002; Smedley and Kinniburgh 2002). Because of the human health risk (Chen et al. 1988; Smith et al. 2002), the US EPA lowered the maximum contaminant level (MCL) for arsenic in drinking water from 50 μg/L to 10 μg/L as As in 2002; compliance with the MCL has been required since 2006 (USEPA 2010. Adsorption has been recognized as a promising technique for removing arsenic from drinking water due to its high removal capacity and ease of operation. However, the relatively high cost of adsorbents with high capacity for arsenic has resulted in high treatment costs, particularly for small water systems (Colby et al. 2010). Oxides such as iron oxide can adsorb arsenic – it is known that adsorption on oxides significantly affects the fate and transport of arsenic in the subsurface (Welch et al. 2003). To take advantage of their high adsorptivity, various metal oxide based adsorbents have been deployed in water treatment systems to remove arsenic (Seigal et al. 2007).

[*]Correspondence: Prof. Ian M. Kennedy, Department of Mechanical and Aerospace Engineering, University of California, Davis, One Shields Avenue, Davis, CA 95616-5294, 530-752-2796, 530-752-4158 FAX, imkennedy@ucdavis.edu.

Since metal oxide nanoparticles often exhibit remarkable adsorption capacities compared to their bulk materials (Mayo et al. 2007; Waychunas et al. 2005), various types of nanostructured metal oxide adsorbents have been developed (Chandra et al. 2010; Hristovski et al. 2008; Yavuz et al. 2006). Cost-effective arsenic removal demands the production of adsorbents (e.g., nanoparticles) that have high adsorption capacities using low cost manufacturing methods. Magnetic adsorbents such as magnetite (Fe_3O_4) nanocrystals (Liu et al. 2008; Mayo et al. 2007; Yavuz et al. 2006), and thiol-functionalized super-paramagnetic nanoparticles (Yantasee et al. 2007) are particularly attractive because of their potential to facilitate solid-liquid separation.

A variety of solution/precipitation techniques have been commonly used to synthesize different types of iron oxides (Cornell and Schwertmann 2003). However, these methods usually utilize a batch process and scale-up may not be straightforward. (Pratsinis 1998). Several aerosol synthesis methods have also been used to produce iron oxides by decomposing iron precursors such as iron pentacarbonyl ($Fe(CO)_5$) in a furnace (Cabanas et al. 1993; Langlet et al. 1986). In contrast, gas-phase flame synthesis is an attractive method for large-scale production of various materials including nanoscale metal oxides (Pratsinis 1998; Wooldridge 1998). Many oxides such as fumed silica, black carbon and alumina have been produced using the method at rates of approximately millions of tons/year (Pratsinis 1998; Stark and Pratsinis 2002). The flame synthesis methods also enable the design of exotic materials such as carbon nanotubes, phosphors, core-shell materials and metal oxides (Kruis et al. 1998; Rosner 2005). The flame synthesis methods are a straightforward and inherently scalable method. In addition, materials that are formed in a gas-phase flame at elevated temperature exhibit high purity (Helble 1998).

There are two common diffusion flame configurations: the normal diffusion flame (DF) configuration and the inverse diffusion flame (IDF) configuration. In the DF configuration, a gaseous fuel is injected into a surrounding flow of oxidizer (air or oxygen-enriched air). Many metal oxides have been synthesized using this flame configuration. In the DF configuration, it is difficult to control oxidation state of the metal oxides because of an abundance of oxygen. In contrast, an oxidizer is injected into a surrounding flow of fuel in the IDF configuration. In the inverse diffusion flame (IDF) configuration, nanoparticles of transition metal oxides can be synthesized with reduced oxidation state. The synthesis of reduced iron oxide nanoparticles in the IDF configuration has been recently reported (Kumfer et al. 2010). The IDF configuration can produce particles with significantly different morphology and crystallinity compared to those synthesized in the DF configuration (Kumfer et al. 2010; Pratsinis et al. 1996). To the best of our knowledge, the arsenic removal capacity of the IONPs synthesized in the gas-phase and their application to arsenic removal from water has not been investigated previously. Solution phase wet chemistry methods have been used in the past – they suffer from difficulty in scale up to commercially significant quantities suitable for widespread use.

Yu et al. (Yu et al. 2004) synthesized magnetite (Fe_3O_4) nanocrystals using a solution of FeO(OH), oleic acid, and 1-octadecene by thermal decomposition of iron carboxylate salts, and Yuvuz et al. (Yavuz et al. 2006) reported that the Fe_3O_4 nanocrystals with the smallest particle size (12 nm) showed the highest arsenic removal capacity. Since gas-phase flame synthesis methods can produce IONPs with different oxidation states, with very small particle sizes, and with different morphologies, they offer the potential for cost effective arsenic removal from water.

The objectives of this study were 1) to characterize iron oxide nanoparticles (IONPs) with tunable oxidation state, synthesized in both the DF and IDF configurations under controlled flame conditions, and to investigate their arsenate (As(V)) removal efficacy, 2) to examine

their applicability in water treatment systems by comparing As(V) removal capacities of the IONPs with those for other iron oxide based adsorbents available commercially (e.g., Bayoxide E33® (E33)) or described in the literature (Chandra et al. 2010; Mayo et al. 2007), and 3) to study the effect of iron oxidation state and other particle characteristics on the As(V) removal capacities of IONPs.

Materials and Methods

Materials

For the synthesis of the IONPs in gas-phase flames, iron pentacarbonyl ($Fe(CO)_5$, AlfaAesar,99.5%) was chosen as the iron precursor. All compressed gases (Ar, O_2, N_2, H_2, CH_4 and C_2H_4) were supplied from Praxair Inc. (San Ramon, CA) with stated purity of 99.5% or higher. In As(V) adsorption isotherm tests, As(V) stock solutions were prepared from reagent grade $Na_2HAsO_4{\cdot}7H_2O$ (AlfaAesar) in deionized water (MilliQ, Millipore Corp., Billerica, MA). The ionic strength of the testing solution was adjusted using sodium nitrate ($NaNO_3$, Sigma Aldrich). HEPES sodium salt (Fisher Scientific) used as a buffer at pH 7 (Kanematsu et al. 2011). All these chemicals were analytical grade and used as received without further purification.

Gas-phase flame synthesis of IONPs

The IONPs were synthesized using either a DF or an IDF configuration, previously described in detail by Guo and Kennedy (Guo and Kennedy 2007) and Kumfer et al. (Kumfer et al. 2010) respectively. Schematics of both the DF and IDF configurations are shown in Figure 1A and 1B, respectively. Six different flames were studied, varying in their configuration and fuel/oxidizer conditions (Table 1). In the DF configuration, the fuel is injected through the central flow line surrounded by an oxidizer flow with or without dilution (Figure 1A) where maghemite, γ-Fe_2O_3, can be synthesized. In contrast, in the IDF configuration, the oxidizer (100% O_2 or O_2 diluted with Ar) was injected through a central annulus of a coannular burner and an outer sheath flow of nitrogen was used to prevent oxygen contamination from room air (Figure 1B). The IDF configuration with different flame conditions (Flame A–E) was used to tune the oxidation state of particles by adjusting flame temperature, oxygen enrichment, fuel dilution, and fuel composition. The flame height was maintained at 30 mm. Iron pentacarbonyl was used as an iron precursor, and H_2 (DF setup) or argon (IDF setup) was bubbled through the liquid precursor at constant temperature; the precursor was maintained in an ice bath at 0° C. The flame synthesized IONPs were collected in a system consisting of a funnel mounted coaxially to the flame, a filter housing assembly, and a vacuum system. The filter assembly housed three 47 mm Teflon filters (J020A047A, Advantec MFS Inc, Dublin CA). The overall particle collection yield ranged from 10 to 100 mg/hr, depending on flame conditions.

Particle Characterization

The synthesized IONPs were suspended in MilliQ water and deposited on a 400 mesh copper TEM grid with a carbon/Formvar film (Ted Pella Inc. Redding CA. Prod # 01754-F); excess liquid was wicked away. The morphology of the IONPs was analyzed by transmission electron microscopy (TEM, Phillips, CM-12). TEM images were taken at an accelerating voltage of 120 kV. The particle crystalline phase was identified using a Scintag powder x-ray diffractometer (XRD) with Cu K_α radiation operated at 45 kV and 40 mA. The powder was scanned for $2\theta = 10° – 80°$ with step size of 0.02° and step scan rate of 2.4 °/min. The average domain size, D_{XRD} was calculated using Scherrer's formula (B. D. Cullity 2001),

$$D_{XRD} = \frac{K\lambda}{\beta \cos\theta} \quad (1)$$

where the shape factor K is 0.9, λ is the incident x-ray wavelength (=1.54 Å), β is the peak full width-half maximum (FWHM) at Bragg angle θ = 35.6°. The BET surface area of the IONPs was obtained using the N_2 adsorption approach (AUTOSORB-1, Quantachrome Instruments, Boynton Beach, FL). Dynamic light scattering was used to determine the particle hydrodynamic size distribution and state of agglomeration/dispersion of the IONPs in water (BIC 90Plus, Brookhaven Instruments, Holtsville, NY). The effective diameter and number-weighted particle size distributions were calculated by the 90Plus software (Brookhaven Instruments). The effective diameter corresponds to the first cumulant of the correlation curve and for multimodal distributions it is weighted roughly by scattering intensity. The number-weighted particle size distribution is approximated by the correlation curve. The particle concentration for the DLS experiment was 50 mg/L in MilliQ (18.2 MΩ-cm) water and the solution was bath sonicated for one minute to disperse the particles. Zeta potential was measured by light scattering (ZetaPlus, Brookhaven Instruments Corp., NY). Particles were suspended in 1 mM KCl with particle concentration of 50 mg/L and the suspension was bath sonicated for five minutes before each sample measurement

Adsorption isotherms

As(V) adsorption isotherm tests were performed in completely mixed batch reactors (15 mL plastic centrifuge vials) at a solid concentration of 1.0 g/L. Duplicates of 10 mL solutions with a fixed amount of solid (10.0 mg) and different initial As(V) concentrations were prepared in the vials. The experiments were conducted at pH 7.0 and ionic strength of 0.02 M. The solution pH was maintained using 1 mM of HEPES, and ionic strength was adjusted using $NaNO_3$. The synthesized IONPs were sonicated for one minute to disperse the particles in the testing solutions using a probe sonicator and then shaken at 300 rpm using a shaker table for 3 days. After shaking, the IONPs were separated by centrifugation. After the separation, supernatants in the samples were carefully collected and acidified with 60% nitric acid and stored at 4°C before analyses. The pH was measured with a glass electrode and a pH meter with three points calibration (Mettle Toledo, Columbus, OH). As(V) concentrations were analyzed using inductively coupled plasma-mass spectrometry (7500i, Agilent Technologies, Wilmington, DE).

Results and Discussion

Particle characterization

The transmission electron microscopy (TEM) images of the six different IONPs as well as a commonly used nanostructured iron oxide adsorbent, Bayoxide E33 (E33), are shown in Figure 2. Particles formed by the DF configuration (i.e., γ-Fe_2O_3) are large compared to the particles formed in the IDF configuration mainly due to higher precursor loading in the DF configuration. For all samples, the images show large aggregates of primary particles. For the IDF configuration, the primary particle size, as determined by XRD, was smallest for sample A and largest for sample D. In contrast to flame-synthesized particles, where the particles are roughly spherical, the commercial sorbent (E33) primary particles are needle-like allowing for large surface area. The BET data for specific surface area for the flame-synthesized samples are shown in Table 2. The IONP synthesized in Flame A has the highest specific surface area of 207 m^2/g, while γ-Fe_2O_3 synthesized in the DF configuration has the lowest of 36 m^2/g. The specific surface area for E33 (158.1 m^2/g) (Kanematsu et al. 2011) is comparable to IONP produced in Flame D. The surface area

weighted diameters D_{SA} (Table 2) are comparable to the primary particle size seen in the TEM images and crystalline size measured by XRD.

The IDF offers a quite different temperature history of particles compared to the DF system. In the latter system, precursors are present in the fuel stream and particles begin to form inside the flame near the reaction zone. They are then convected through the flame. The high temperature promotes sintering at the relatively low melting point of γ – Fe2O3. On the other hand, the IDF drives freshly nucleated particles away from the flame into cold gases by thermophoresis and the particles have no opportunity to sinter and grow. The IDF configuration is ideal for the production of very small, high surface area, aerosols as Zhu and Pratsinis (1997) found in study of SiO2 and SnO2 synthesis in DF and IDF configurations.

Add this reference: Synthesis of SiO2 and SnO2 particles in diffusion flame reactors, Wenhua Zhu and Sotiris E. Pratsinis, AIChE J. 43, pp 2657 – 2664 (1997).

Powder XRD spectra for several samples are shown in Figure 3. The spectra show peaks for spinel ferrites. Because this spinel structure is characteristic of both maghemite and magnetite, it is hard to distinguish between these ferrites. The crystalline diameter, D_{XRD}, is determined by eq. 1 and these data are also shown in Table 2. In general, the particle size increases with increasing flame temperature.

The distribution of hydrodynamic diameters as measured by DLS is shown in Figure S1 (the supporting information). The mean particle size in solution for all samples is larger than the primary particle size seen in the TEM images, confirming that the particles form aggregates in solution. For samples produced in Flames A–E, the size distributions are broad – and Flames B and D produced IONPs with a bimodal distribution. Although TEM images of γ-Fe_2O_3 show a distinct bimodal distribution as observed previously by Guo and Kennedy (Guo and Kennedy 2007), DLS data do not reflect this bimodality. Since scattering intensity is proportional to d^6, the scattering signal from large particles will dominate signals from smaller particles and this likely explains the apparent absence of the small particle mode from the DLS data. The mean number-weighted diameter and intensity-weighted diameter data are also shown in Table 2.

To quantify the oxidation states of iron in the IONPs synthesized in Flames A–E, Kumfer et al. (Kumfer et al. 2010) used XANES spectroscopy to analyze IONPs produced under identical conditions; they compared sample spectra to standard reference materials such as Fe(0) foil, magnetite, and Fe(III) oxides. The results from their XANES data are summarized in Table 2. Both γ-Fe_2O_3 synthesized in the DF configuration and the IONP synthesized in Flame A have only Fe(III) valence. The IONPs synthesized in Flames B, C, and D have increasing Fe(II) content, and the IONP synthesized in Flame E includes zero valent iron (ZVI) along with Fe(II) and Fe(III). Further evidence of mixed oxidation states in the IONPs synthesized in Flames B – D is provided by magnetic data obtained using a vibrating sample magnetometer (VSM)(Kumfer et al. 2010). The slight coercive force measured for all particles (Table 2) can be attributed to a non-monodispersed particle distribution; a few large particles in the distribution contribute to the coercivity

The values of the zeta potential of the IONPs at pH 7 are listed in Table 2. The zeta potential, an approximation to the surface potentials of particles in solution, was high (> 30 mV) for the IONPs synthesized in Flames A, D and E, suggesting electrostatic stabilization of the particles in solution. In contrast, the IONPs synthesized in Flames B, C and the DF configurations showed lower zeta potentials, indicating lower particle stability.

As(V) removal capacity

As(V) adsorption isotherms were obtained at pH 7 for the six different IONPs and compared with a commonly used goethite-based adsorbent (E33) (Kanematsu et al. 2010) and Fe_3O_4 nanocrystals synthesized by thermal decomposition of iron carboxylate salts (Yavuz et al. 2006) in Figure 4A. On a mass basis (Figure 4A), As(V) adsorption capacities of the six IONPs are rated as follows: Flame A > Flame B > Flame E > Flame C > Flame D > γ-Fe_2O_3 synthesized in the DF configuration. Hence, it is found that the IDF-IONPs have much higher As(V) adsorption capacities than that of the DF-IONP. Almost all IDF-IONPs showed higher adsorption capacity than that of E33 on a mass basis. The adsorption capacity of the fully oxidized IDF-IONPs synthesized in Flame A, maghemite (γ-Fe_2O_3), is three to four times higher than that of E33 on a mass basis. Therefore, the IDF-IONPs synthesized in Flame A could be used for As(V) removal in water based on their As(V) adsorption capacity. In contrast, γ-Fe_2O_3 synthesized in the DF configuration showed much lower adsorption capacity than E33, although its chemical composition is identical to the IDF-IONPs synthesized in Flame A. This is probably due to much larger particle size of γ-Fe_2O_3 synthesized in the DF configuration.

The specific surface area normalized adsorption isotherms are shown in Figure 4B. The specific surface area normalized adsorption capacity of γ-Fe_2O_3 synthesized in the DF configuration is quite similar to that of the IDF-IONPs synthesized in Flame A (Figure 4B). Therefore, the difference in the adsorption capacity between these two materials is due to different particle sizes rather than differences in the number of active surface sites per area. It may be possible, therefore, that the DF configuration could produce IONPs with high adsorption capacity if their particle sizes were reduced to below approximately 10 nm by controlling the flame characteristics.

Yavuz et al. (Yavuz et al. 2006) synthesized monodisperse Fe_3O_4 nanocrystals with different particle sizes (12, 20, and 300 nm) and demonstrated their As(V) and As(III) removal capacities at pH 8. In their studies, the Fe_3O_4 nanocrystals were synthesized using a mixture of FeO(OH), oleic acid, and 1-octadecene by thermal decomposition of iron carboxylate salts as described in Yu et al. (Yu et al. 2004). The size of the Fe_3O_4 nanocrystals strongly affected arsenic removal capacities, and the Fe_3O_4 nanocrystals with 12 nm diameter showed the highest adsorption capacity, which is equivalent to approximately two hundred times higher arsenic removal capacity than commercially available Fe_3O_4 nanoparticles (Yean et al. 2005). As(V) adsorption isotherms of the six different IONPs at pH 7 are compared with that of Yavuz et al. 12 nm Fe_3O_4 nanocrystals at pH 8 in Figure 4A. Although As(V) adsorption on iron oxide decreases with increasing pH (Dixit and Hering 2003; Gimenez et al. 2007), the IDF-IONPs generally offer superior As(V) removal compared with the magnetite (Fe_3O_4) nanocrystals synthesized by Yavuz et al. (Yavuz et al. 2006), especially at very low arsenic concentrations.

Effect of oxidation state on As(V) removal capacity of IONPs

The oxidation states of iron in the IDF-IONPs were determined previously by our laboratory using XANES (Kumfer et al. 2010). The effect of oxidation state of the IDF-IONPs on their As(V) surface area normalized removal capacities at three different As(V) concentrations (10, 100, and 1,000 μg/L as As) is shown in Figure 5. The Fe(II)/Fe(III) ratio is used as an indication of the oxidation state of iron in the IONPs. It can be seen that As(V) adsorption capacity increased with a decrease in Fe(II)/Fe(III) for the IDF-IONPs. Since Su and Puls (Su and Puls 2008) reported that no chemical reduction of As(V) could be observed in magnetite suspensions, chemical reduction of As(V) to As(III) is probably not the reason for the lower As(V) adsorption on more reduced IONPs. Although the data in Figure 5 are suggestive of an effect of iron oxidation state on adsorption capacity, unambiguous

conclusions about this effect cannot be derived from our data because there is a strong cross-correlation between the oxidation state and the specific surface area of the particles in moving from material A to material D. Even though the data in Figure 4B have been normalized by specific surface area this may not completely remove the effect of surface area because arsenate accessible surface area in solution may differ from nitrogen accessible surface area under vacuum. Differences in zeta potential reflect differences in surface potentials but may also be related to particle aggregation during the batch experiments. Further, the IONPs synthesized in Flame E, which contains 14% of Fe(0) and 12% of Fe(II), did not follow the trend in Figure 5, instead exhibiting a slightly higher adsorption capacity than the more oxidized IDF-IONPs synthesized in Flames C and D (Figures 4A and 4B). Kanel et al. (Kanel et al. 2005) reported that ZVI is susceptible to oxidation in water and gradually oxidized to magnetite and/or maghemite corrosion products mixed with lepidocrocite (γ-FeO(OH)) over 60 days. The magnetite/maghemite products derived from oxidized ZVI might contribute to the increase in As(V) adsorption capacity for the IONPs synthesized in Flame E. Moreover, the IONPs synthesized in Flame E also showed higher zeta potential at pH 7.0 than the IONPs synthesized in Flames C and D. The reason for the higher zeta potential of this IONP is not clear.

Conclusion

This study demonstrates that IONPs synthesized in flames are promising adsorbents for the removal of As(V) from water with the additional attractive property of magnetization that can be used for separation and manipulation. An increase in the Fe(III)/Fe(II) ratio resulted in a higher arsenic adsorption capacity, with fully oxidized iron oxide (Flame A) particles showing an approximately four-fold increase in adsorption capacity compared to a commercial sorbent (Bayoxide E33). Although inverse diffusion flames are capable of producing low oxidation state particles, their major benefit in the case of As adsorption is their ability to yield very small, unsintered particles that lead to high surface area materials. A normal diffusion flame (DF) can also produce maghemite but with significantly lower specific surface area. Since flame synthesis has significant potential for economical large-scale production of IONPs, adoption of an IDF synthesis route may lead to reduction in the currently high cost of adsorption systems for arsenic removal from water (Colby et al. 2010).

Acknowledgments

The project described was supported by Award Number P42ES004699 from the National Institute of Environmental Health Sciences. The content is solely the responsibility of the authors and does not necessarily represent the official views of the National Institute of Environmental Health Sciences or the National Institutes of Health. Contributions by MK to the project were supported under contract #06-55254 from the California Department of Public Health, Safe Drinking Water Revolving Fund. The content is solely the responsibility of the authors and does not necessarily represent the official views of the National Institute of Environmental Health Sciences, the National Institutes of Health, or the California Department of Public Health.

References

AdEdge Technologies Inc. Buford GA USA:

Cullity, BD.; SRS. Elements of X-Ray Diffraction. Addison-Wesley; 2001.

Cabanas MV, Valletregi M, Labeau M, Gonzalezcalbet JM. Spherical iron-oxide particles synthesized by an aerosol technique. Journal of Materials Research. 1993; 8:2694–2701.

Chandra V, Park J, Chun Y, Lee JW, Hwang I-C, Kim KS. Water-dispersible magnetite-reduced graphene oxide composites for arsenic removal. ACS NANO. 2010; 4:3979–3986. [PubMed: 20552997]

Chen CJ, Kuo TL, Wu MM. Arsenic and cancers. Lancet. 1988; 1:414–415. [PubMed: 2893213]

Colby EJH, Young TM, Green PG, Darby JL. Costs of arsenic treatment for potable water in California and comparison to U.S. Environmental Protection Agency affordability metrics. Journal of the American Water Resources Association. 2010; 46:1238–1254.

Cornell, RM.; Schwertmann, U. The iron oxides : Structure, properties, reactions, occurrences, and uses. Weinheim: Wiley-VCH; 2003.

Dixit S, Hering J. Comparison of arsenic(V) and arsenic(III) sorption onto iron oxide minerals: Implications for arsenic mobility. Environmental Science and Technology. 2003; 37:4182–4189. [PubMed: 14524451]

Gimenez J, Martinez M, de Pablo J, Rovira M, Duro L. Arsenic sorption onto natural hematite, magnetite, and goethite. Journal of Hazardous Materials. 2007; 141:575–580. [PubMed: 16978766]

Guo B, Kennedy IM. Gas-phase flame synthesis and characterization of iron oxide nanoparticles for use in a health effects study. Aerosol Science and Technology. 2007; 41:944–951.

Helble JJ. Combustion aerosol synthesis of nanoscale ceramic powders. Journal of Aerosol Science. 1998; 29:721–736.

Hristovski KD, Westerhoff PK, Crittenden JC, Olsow LW. Arsenate removal by nanostructured ZrO2 spheres. Environmental Science & Technology. 2008; 42:3786–3790. [PubMed: 18546723]

Kanel SR, Manning B, Charlet L, Choi H. Removal of arsenic(III) from groundwater by nanoscale zero-valent iron. Environmental Science & Technology. 2005; 39:1291–1298. [PubMed: 15787369]

Kanematsu M, Young TM, Fukushi K, Green PG, Darby JL. Extended triple layer modeling of arsenate and phosphate adsorption on a goethite-based granular porous adsorbent. Environmental Science and Technology. 2010; 44:3388–3394. [PubMed: 20355701]

Kanematsu M, Young TM, Fukushi K, Sverjensky DA, Green PG, Darby JL. Quantification of the effects of organic and carbonate buffers on arsenate and phosphate adsorption on a goethite-based granular porous adsorbent. Environmental Science & Technology. 2011; 45:561–568. [PubMed: 21158435]

Kruis FE, Fissan H, Peled A. Synthesis of Nanoparticles in the Gas Phase for Electronic, Optical and Magnetic Applications - A Review. J. Aerosol. Sci. 1998; 29:511–535.

Kumfer BM, Shinoda K, Jeyadevan B, Kennedy IM. Gas-phase flame synthesis and properties of magnetic iron oxide nanoparticles with reduced oxidation state. Journal of Aerosol Science. 2010; 41:257–265. [PubMed: 20228941]

Langlet M, Labeau M, Bochu B, Joubert JC. Preparation of thin-films in the system g-Fe2O3-Fe3O4 for recording media by spray pyrolysis of organometallic solutions using an ultrasonic pump. IEEE Transactions on Magnetics. 1986; 22:151–156.

Liu JF, Zhao ZS, Jiang GB. Coating Fe3O4 magnetic nanoparticles with humic acid for high efficient removal of heavy metals in water. Environmental Science & Technology. 2008; 42:6949–6954. [PubMed: 18853814]

Mayo JT, Yavuz C, Yean S, Cong L, Shipley H, Yu W, Falkner J, Kan A, Tomson M, Colvin VL. The effect of nanocrystalline magnetite size on arsenic removal. Science and Technology of Advanced Materials. 2007; 8:71–75.

Nordstrom DK. Public health - Worldwide occurrences of arsenic in ground water. Science. 2002; 296:2143–2145. [PubMed: 12077387]

Pratsinis SE. Flame aerosol synthesis of ceramic powders. Progress in Energy and Combustion Science. 1998; 24:197–219.

Pratsinis SE, Zhu WH, Vemury S. The role of gas mixing in flame synthesis of titania powders. Powder Technology. 1996; 86:87–93.

Rosner DE. Flame synthesis of valuable nanoparticles: Recent progress/current needs in areas of rate laws, population dynamics, and characterization. Ind. Eng. Chem. Res. 2005; 44:6045–6055.

Seigal, M.; Aragon, A.; Zhao, H.; Everett, R.; Aragon, M.; Nocon, M.; Dwyer, B.; Marbury, J.; Kirby, C.; North, K. Pilot test of arsenic adsorptive media treatment technologies at Socorro Springs. Albuquerque: Sandia National Laboratories; 2007.

Smedley PL, Kinniburgh DG. A review of the source, behaviour and distribution of arsenic in natural waters. Applied Geochemistry. 2002; 17:517–568.

Smith AH, Lopipero PA, Bates MN, Steinmaus CM. Public health - Arsenic epidemiology and drinking water standards. Science. 2002; 296:2145–2146. [PubMed: 12077388]

Stark WJ, Pratsinis SE. Aerosol flame reactors for manufacture of nanoparticles. Powder Technology. 2002; 126:103–108.

Su CM, Puls RW. Arsenate and arsenite sorption on magnetite: Relations to groundwater arsenic treatment using zerovalent iron and natural attenuation. Water Air and Soil Pollution. 2008; 193:65–78.

Sverjensky DA. Prediction of surface charge on oxides in salt solutions: Revisions for 1:1 (M^+L^-) electrolytes. Geochimica et Cosmochimica Acta. 2005; 69:225–257.

USEPA. U.SEnvironmental Protection Agency, Arsenic in drinking water. 2010. Available at http://water.epa.gov/lawsregs/rulesregs/sdwa/arsenic/index.cfm.

Waychunas GA, Kim CS, Banfield JF. Nanoparticulate iron oxide minerals in soils and sediments: unique properties and contaminant scavenging mechanisms. Journal of Nanoparticle Research. 2005; 7:409–433.

Welch, AH.; Stollenwerk, KG. ebrary Inc. Arsenic in ground water. Boston: Kluwer Academic Publishers; 2003.

Wooldridge MS. Gas-phase combustion synthesis of particles. Progress in Energy and Combustion Science. 1998; 24:63–87.

Yantasee W, Warner CL, Sangvanich T, Addleman RS, Carter TG, Wiacek RJ, Fryxell GE, Timchalk C, Warner MG. Removal of heavy metals from aqueous systems with thiol functionalized superparamagnetic nanoparticles. Environmental Science & Technology. 2007; 41:5114–5119. [PubMed: 17711232]

Yavuz CT, Mayo JT, Yu WW, Prakash A, Falkner JC, Yean S, Cong LL, Shipley HJ, Kan A, Tomson M, Natelson D, Colvin VL. Low-field magnetic separation of monodisperse Fe3O4 nanocrystals. Science. 2006; 314:964–967. [PubMed: 17095696]

Yean S, Cong L, Yavuz CT, Mayo JT, Yu WW, Kan AT, Colvin VL, Tomson MB. Effect of magnetite particle size on adsorption and desorption of arsenite and arsenate. J. Mater. Res. 2005; 20:3255–3264.

Yu WW, Falkner JC, Yavuz CT, Colvin VL. Synthesis of monodisperse iron oxide nanocrystals by thermal decomposition of iron carboxylate salts. Chemical Communications. 2004:2306–2307. [PubMed: 15489993]

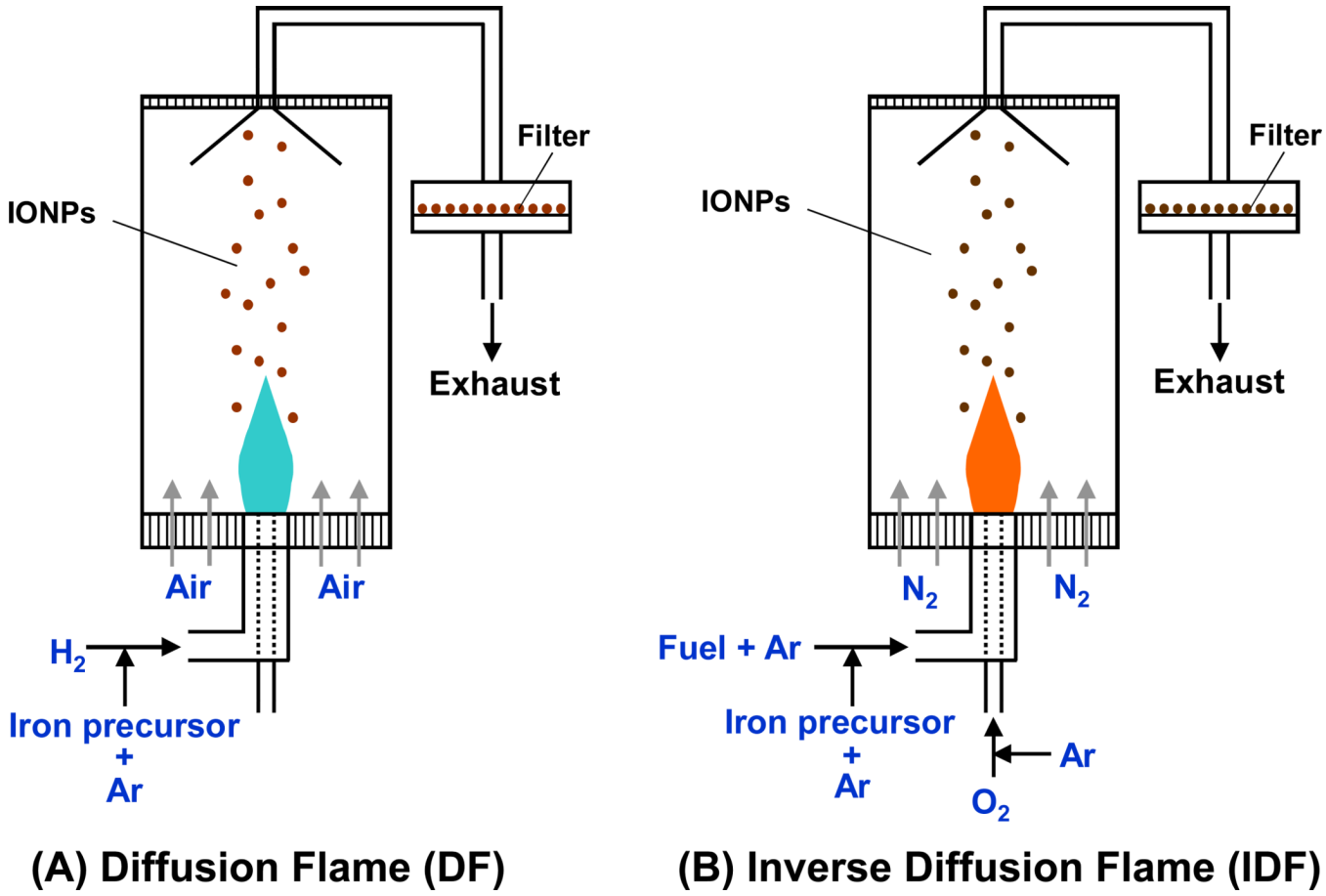

Figure 1.
Schematic of the flame configurations to synthesize iron oxide nanoparticles (IONPs). In the diffusion flame (DF) configuration (A), the fuel is injected into the center annulus with air on the outside. In the inverse diffusion flame (IDF) configuration (B), the oxidizer is injected into the center annulus with fuel injected in the outside concentric flow.

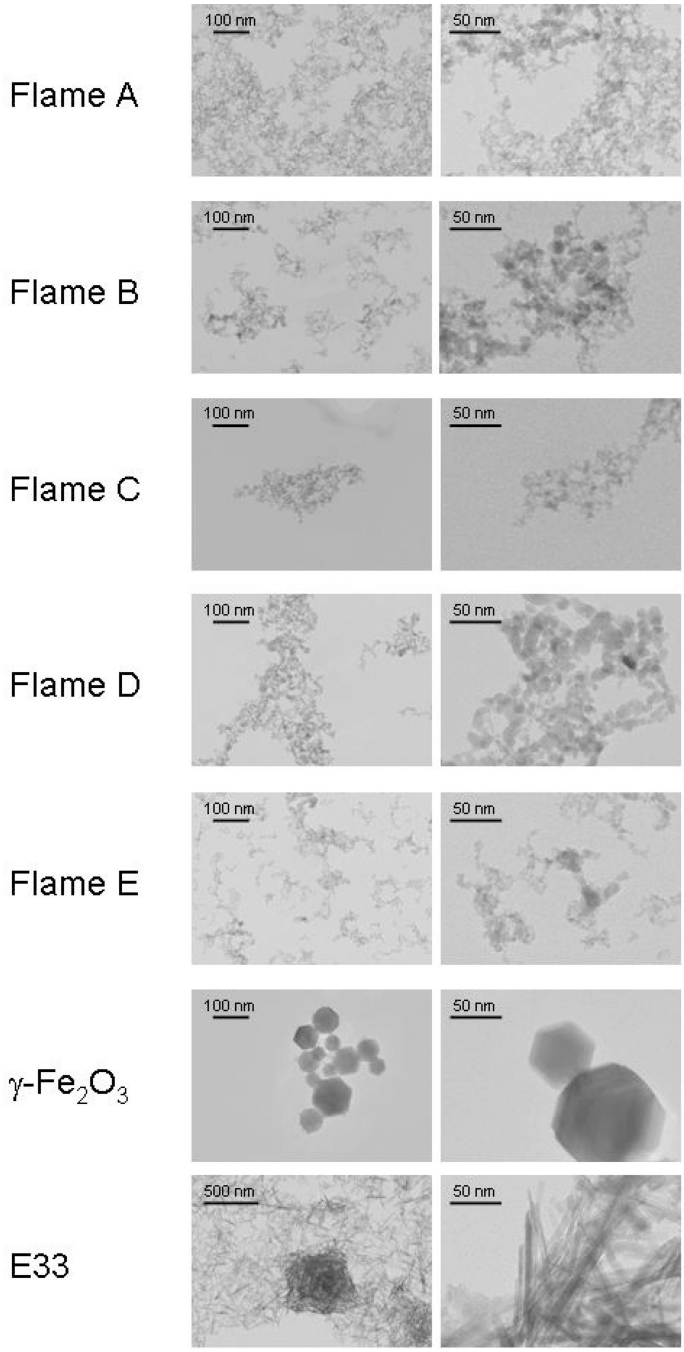

Figure 2.
Transmission electron microscope (TEM) images of the flame-synthesized IONPs (Flames A–E correspond to the IONPs synthesized in the IDF configuration, and maghemite, γ-Fe_2O_3 corresponds to the IONPs synthesized in the DF configuration) and a goethite-based commercial sorbent (E33). For all samples, the particles form large aggregates composed of smaller primary particles.

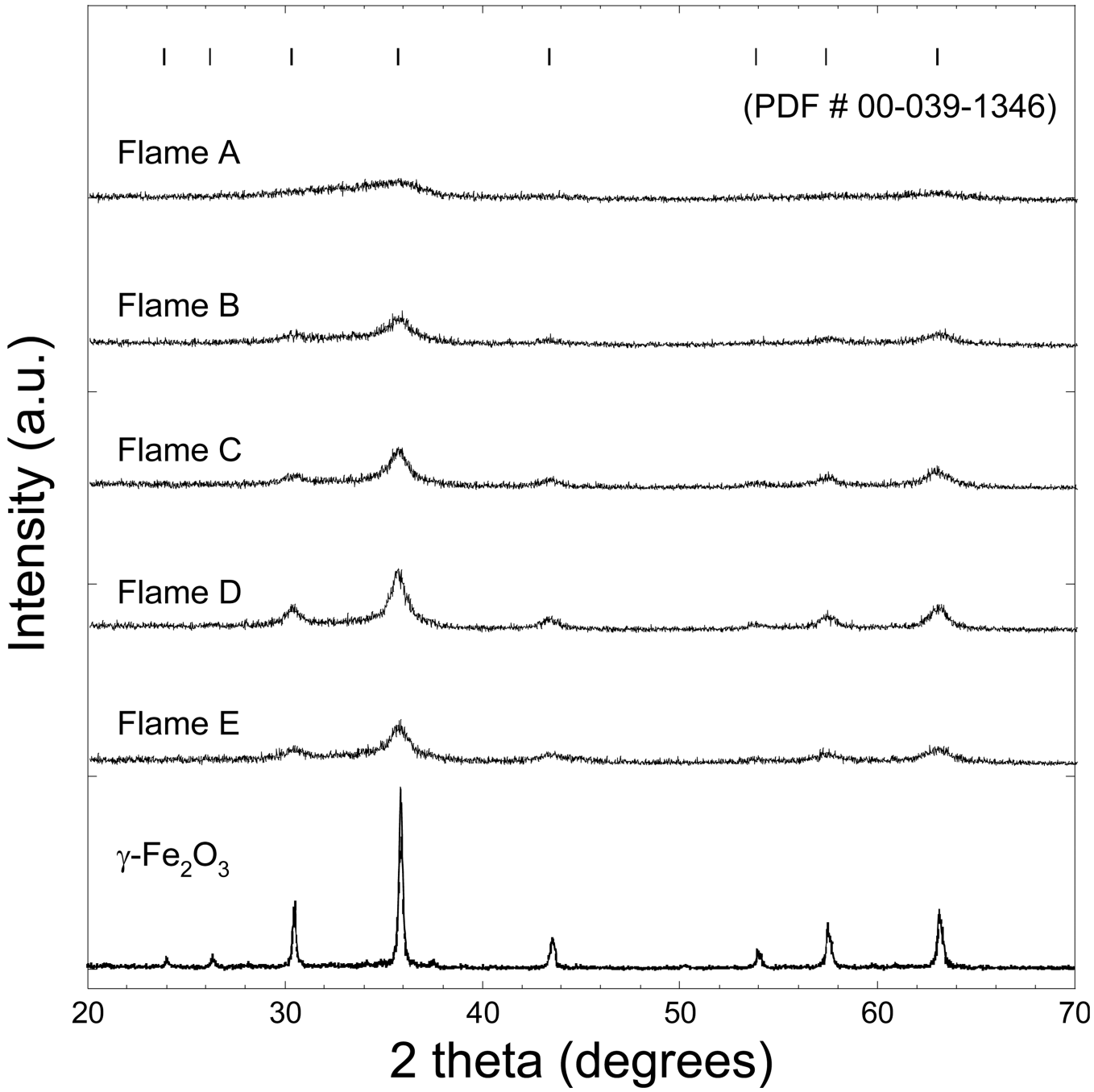

Figure 3.
Powder X-ray diffraction patterns of flame synthesized iron oxide samples. Vertical ticks represent main diffraction peaks for maghemite.

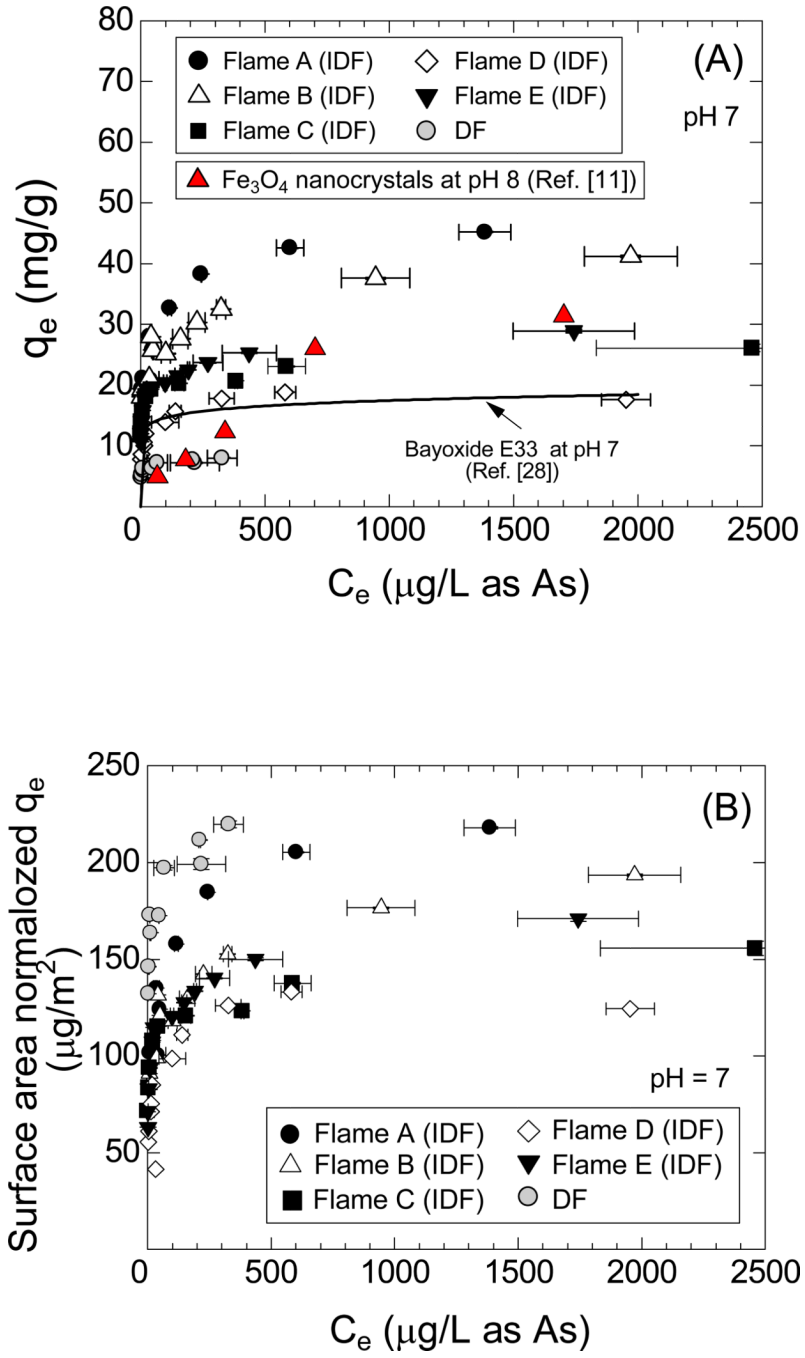

Figure 4.

(A) As(V) adsorption isotherms of the flame-synthesized IONPs at pH 7. As(V) adsorption isotherms of Fe_3O_4 nanocrystals (Yavuz et al. 2006) and a goethite-based common adsorbent, E33(Kanematsu et al. 2011) are included for reference. (B) Surface area normalized As(V) adsorption isotherms of the flame synthesized IONPs at pH 7.

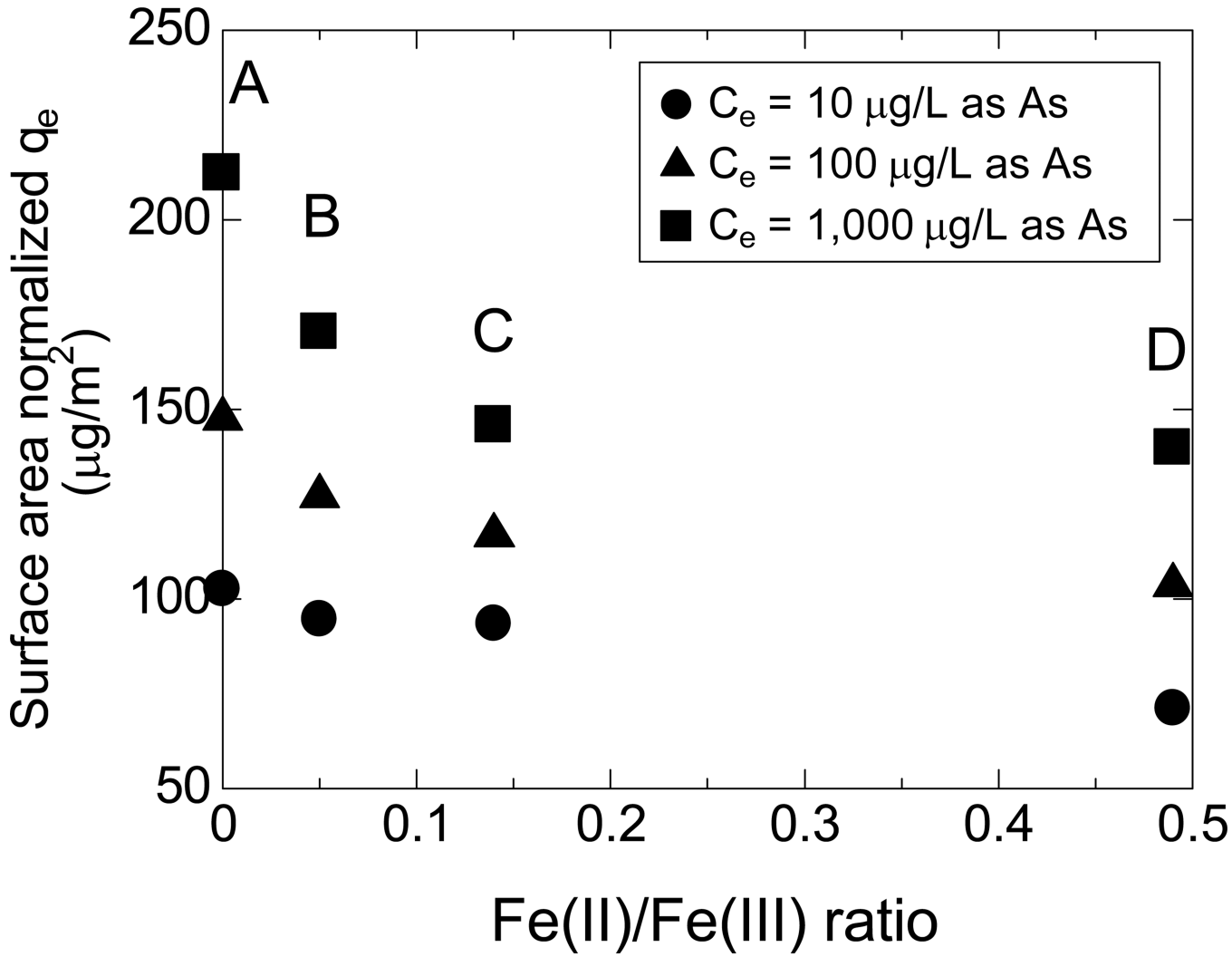

Figure 5.
Influence of oxidation state, indicated by Fe(II)/Fe(III) ratio, on the surface area normalized As(V) adsorption capacity of the IONPs (Flames A to D) at three different liquid phase equilibrium As(V) concentrations.

Table 1

Flow conditions used to synthesize iron oxide nanoparticles.

Sample Name	Flame configuration[1]	Fuel	Oxidizer	Fuel line flow rate (L/min)			Oxidizer line flow rate (L/min)		T_{ad} (K)[2]
				Fuel	Ar	$Ar_{precursor}$	O_2	Ar	
γFe_2O_3	DF	H_2	Air	0.1	-	-	0.1	-	2200
Flame A	IDF	CH_4	O_2	0.204	0.983	0.013	0.14	0.56	2150
Flame B	IDF	CH_4	O_2	0.084	1.103	0.013	0.128	0.043	2150
Flame C	IDF	CH_4	O_2	0.12	1.067	0.013	0.19	-	2450
Flame D	IDF	CH_4	O_2	0.18	1.007	0.013	0.25	-	2650
Flame E	IDF	C_2H_4	O_2	0.072	1.115	0.013	0.129	0.021	2450

[1] DF, diffusion flame; IDF, inverse diffusion flame.

[2] data from Kumfer *et al.* Kumfer et al. 2010) except, for γ-Fe_2O_3, data from Guo and Kennedy (2007).

Table 2

Summary of particle properties.

Sample Name	BET Surface Area (m^2/g)	D_{SA} (nm)	D_{XRD} (nm)	D_{NWM} (nm)[1]	D_{IWM} (nm)[2]	M_S (emu/g)[3]	Hc (Oe)[3]	ζ (mV)	Percent of total iron in iron oxides[3]		
									Fe(0)	Fe(II)	Fe(III)
γ-Fe_2O_3	36	29	36	325.7	387.8	n/a	n/a	2.4	-	-	100
Flame A	207	4.9	2.9[3]	63.6	144.2	6.5	13	35.0	-	-	100
Flame B	213	4.8	7.9[3]	88.2	195.0	24	19	12.9	-	~5	~95
Flame C	168	6.4	11[3]	124.7	293.8	42	30	7.4	-	12	88
Flame D	141	8.2	12[3]	83.5	209.4	57	60	34.6	-	33	67
Flame E	169	6.0	n/a	74.7	150.6	60	76	30.5	14	10	76

[1] Number weighted mean diameter.

[2] Intensity weighted mean diameter.

[3] data from Kumfer et al. (Kumfer et al. 2010)

Aerosol Sci Technol. Author manuscript; available in PMC 2013 May 01.